

Optical Engineering

OpticalEngineering.SPIEDigitalLibrary.org

Simplex ACE: a constrained subspace detector

Amanda Ziemann
James Theiler



Amanda Ziemann, James Theiler, "Simplex ACE: a constrained subspace detector," *Opt. Eng.* **56**(8), 081808 (2017), doi: 10.1117/1.OE.56.8.081808.

Simplex ACE: a constrained subspace detector

Amanda Ziemann* and James Theiler

Los Alamos National Laboratory, Intelligence and Space Research Division, Space Data Science and Systems Group, Los Alamos, New Mexico, United States

Abstract. In hyperspectral target detection, one must contend with variability in both target materials and background clutter. While most algorithms focus on the background clutter, there are some materials for which there is substantial variability in the signatures of the target. When multiple signatures can be used to describe a target material, subspace detectors are often the detection algorithm of choice. However, as the number of variable target spectra increases, so does the size of the target subspace spanned by these spectra, which in turn increases the number of false alarms. Here, we propose a modification to this approach, wherein the target subspace is instead a constrained subspace, or a simplex without the sum-to-one constraint. We derive the simplex adaptive matched filter (simplex AMF) and the simplex adaptive cosine estimator (simplex ACE), which are constrained basis adaptations of the traditional subspace AMF and subspace ACE detectors. We present results using simplex AMF and simplex ACE for variable targets, and compare their performances against their subspace counterparts. Our primary interest is in the simplex ACE detector, and as such, the experiments herein seek to evaluate the robustness of simplex ACE, with simplex AMF included for comparison. Results are shown on hyperspectral images using both implanted and ground-truthed targets, and demonstrate the robustness of simplex ACE to target variability. © 2017 Society of Photo-Optical Instrumentation Engineers (SPIE) [DOI: 10.1117/1.OE.56.8.081808]

Keywords: hyperspectral; target detection; simplex detectors; subspace detectors; adaptive cosine estimator; matched filter.

Paper 170151SS received Feb. 1, 2017; accepted for publication May 9, 2017; published online Jun. 15, 2017.

1 Introduction

Given a hyperspectral image of a scene and one or more spectral signatures corresponding to a material of interest (i.e., the target), the goal of target detection is to locate occurrences of that material in the scene. The images are usually captured from aerial or satellite-based platforms and can aid in numerous civilian and military applications. When the target material has relatively stable spectral features, e.g., as with a gas-phase chemical plume,^{1–5} it can be well-characterized by a single spectral signature; in such a case, the detection approaches are more straightforward but still challenging due to atmospheric variability and background clutter.^{6–9} Here, our focus is on targets with more substantial intrinsic spectral variability, e.g., due to differences in particle morphology.^{10–12} When a target material is represented with a library of multiple spectra, subspace detectors are often used^{13–16} to capture this variability through a linear target subspace. This can work well for a small number of spectra, but as more target spectra are used (i.e., a large spectral library), the target subspace can become so large that the detectors become completely ineffective. By constraining the target subspace to only allow nonnegative linear combinations of the input target spectra, rather than all linear combinations, the target space becomes much more stable to increasing numbers of variable target spectra. Our approach follows earlier work by Adler-Golden et al.,¹⁷ which explored the notion of using constrained low-dimensional target subspaces, as well as work by Broadwater et al.,^{18,19} which implemented linear unmixing on both the background and target endmembers in order to compute physical target abundances.

This paper is organized as follows. Section 2 provides an overview of hyperspectral imaging (HSI). Section 3 presents

traditional target detection approaches, as well as a derivation of the simplex detectors. Section 4 describes the experiments conducted here and their results. Section 5 concludes with a discussion of the merits of simplex adaptive cosine estimator (simplex ACE), in comparison to several alternative approaches.

2 Hyperspectral Imaging

Images that are captured with a standard digital camera have three values associated with each image pixel: how red that portion of the scene is, how green it is, and how blue it is. While we traditionally design our digital cameras to mimic how our eyes see, we are capable of digitally imaging scenes at a larger number of wavelengths and at finer spectral resolutions. In HSI, scenes are imaged at hundreds of narrow, contiguous wavelength bands, often in both the visible and nonvisible regimes (starting in the ultraviolet, and ranging up through short-wave, midwave, and long-wave infrared). For an image captured at d wavelengths, each pixel in the image can be represented as a vector in \mathbb{R}^d . This provides a natural Euclidean-space representation for the data, where the axes correspond to specific wavelengths, and the associated vector elements correspond to reflectance or radiance values at those wavelengths.

The advantage of the higher number of wavelengths in HSI is that materials that may visibly appear very similar, such as a green vehicle in a grass field, will “look” very different spectrally. This ability to distinguish between materials (e.g., water, vegetation, chemicals, road systems, etc.) is the crux of HSI analysis. There are a variety of applications that leverage remote material discrimination, including scene classification,^{20,21} broad area search,²² anomaly detection,^{23,24}

*Address all correspondence to: Amanda Ziemann, E-mail: ziemann@lanl.gov

change detection,^{25,26} and target detection,^{14,27–32} the last of which is the focus of this paper.

3 Target Detection

The research described here is motivated by the hyperspectral target detection, but the target detection techniques presented in this section, along with the derived simplex ACE and simplex adaptive matched filter (simplex AMF) detectors, may be applicable to a broader array of signal detection problems, including radar, LIDAR, radio frequency etc.

3.1 Single-Input Target Detection

In the framework for single-input target detection, one representative target spectrum is used to search over an image and assign a detection score to each pixel. This section summarizes established detectors for such a framework. Here, to simplify the mathematical exposition, we assume that both the image data and target data have already been whitened using the image (i.e., background) covariance matrix $R \in \mathbb{R}^{d \times d}$ where d is the dimensionality of the pixels, i.e., the number of spectral bands. Note that we do not mean-subtract the data, as global mean subtraction is most appropriate for the additive target model. Our interest is in solid targets, which obscure or partially obscure the background and, therefore, are not strictly additive with respect to the background.^{33,34}

Given target signature $\mathbf{s} \in \mathbb{R}^d$ and pixel measurement $\mathbf{x} \in \mathbb{R}^d$, the AMF detector^{35–37} is the length of the projection of \mathbf{x} in the \mathbf{s} direction

$$\text{AMF: } \mathcal{D}(\mathbf{x}) = \frac{\mathbf{s}^\top \mathbf{x}}{\|\mathbf{s}\|} = \frac{\mathbf{s}^\top \mathbf{x}}{\sqrt{\mathbf{s}^\top \mathbf{s}}}. \quad (1)$$

And the adaptive cosine (sometimes “coherence”) estimator^{38,39} is given by the squared cosine of the angle θ between \mathbf{s} and \mathbf{x}

$$\text{ACE: } \mathcal{D}(\mathbf{x}) = \cos^2 \theta = \frac{(\mathbf{s}^\top \mathbf{x})^2}{\|\mathbf{s}\|^2 \|\mathbf{x}\|^2}. \quad (2)$$

In the ACE formulation described above, the decision surfaces are conical surfaces pointing in both the positive and negative directions of the (whitened) target. We include this variant of ACE because it can be extended to subspace detection; however in practice, the “one-sided” variant of ACE—which distinguishes negative-direction decision

Table 1 Notation.

$d \in \mathbb{N}$	Dimensionality of pixels; number of spectral bands
$\mathbf{x} \in \mathbb{R}^d$	Image pixel under test
$\mathbf{s} \in \mathbb{R}^d$	Single target vector
$k \in \mathbb{N}$	Dimensionality of target subspace
$S \in \mathbb{R}^{d \times k}$	Matrix describing subspace (columns are target basis vectors); generally, $k < d$
$\mathbf{a} \in \mathbb{R}^k$	Coefficient vector corresponding to target strengths and/or abundances; note that $S\mathbf{a}$ is a specific target subspace vector
$R \in \mathbb{R}^{d \times d}$	Background covariance matrix

surfaces from positive-direction decision surfaces—is generally preferable for single-input target detection.⁴⁰ This formulation is given by the unsquared cosine

$$\text{ACE}^+: \mathcal{D}(\mathbf{x}) = \cos \theta = \frac{\mathbf{s}^\top \mathbf{x}}{\|\mathbf{s}\| \|\mathbf{x}\|} = \frac{\mathbf{s}^\top \mathbf{x}}{\sqrt{\mathbf{s}^\top \mathbf{s}} \sqrt{\mathbf{x}^\top \mathbf{x}}}. \quad (3)$$

3.2 Multiple-Input Target Detection

The framework for multiple-input target detection uses a library of target spectra to search over an image and assign each pixel a detection score. A common representation of multiple target spectra is as a linear target subspace,^{13,15,41} and once again, we are assuming here that both the targets and image have been whitened by R .

Let the matrix $S \in \mathbb{R}^{d \times k}$ describe the target subspace, where k is the dimensionality of the target subspace, and the columns of S are the (not necessarily orthogonal) basis vectors. An element of the subspace is a linear combination of these basis vectors; writing $\mathbf{s} = S\mathbf{a}$ is saying that the target vector \mathbf{s} is the sum of vectors that are columns of S , with weights given by the components of \mathbf{a} . Here, \mathbf{a} is the coefficient vector corresponding to target strengths and/or abundances; note that $S\mathbf{a}$ is a specific target subspace vector.

Although we do not need the columns of S to be orthogonal, we require that they be linearly independent; in that case, $S^\top S$ is a full rank and therefore invertible matrix. Consider the projection operator

$$P_s = S(S^\top S)^{-1} S^\top. \quad (4)$$

It is simple to show that $P_s P_s = P_s$, that $P_s^\top = P_s$, and that for any pixel \mathbf{x} , the projection $P_s \mathbf{x}$ is in the subspace S . The latter statement follows from writing $P_s \mathbf{x} = S(S^\top S)^{-1} S^\top \mathbf{x} = S\mathbf{a}$ for $\mathbf{a} = (S^\top S)^{-1} S^\top \mathbf{x}$. For vectors that are already in the subspace, and thus can be written as $S\mathbf{a}$, then it follows that $P_s S\mathbf{a} = S(S^\top S)^{-1} S^\top S\mathbf{a} = S\mathbf{a}$. So, the projection operator has no effect inside the subspace.

An alternative way to think about this projection operator is that it maps the vector \mathbf{x} to the vector in the subspace S that is closest to \mathbf{x} . That is, $P_s \mathbf{x} = S\mathbf{a}_x$, where

$$\mathbf{a}_x = \operatorname{argmin}_{\mathbf{a}} \|\mathbf{x} - S\mathbf{a}\| = \operatorname{argmin}_{\mathbf{a}} (\mathbf{x} - S\mathbf{a})^\top (\mathbf{x} - S\mathbf{a}). \quad (5)$$

This equation finds \mathbf{a}_x such that the distance between \mathbf{x} and the corresponding subspace element $S\mathbf{a}_x$ is minimized; it is straightforward to show that the solution to this minimization is given by $\mathbf{a}_x = (S^\top S)^{-1} S^\top \mathbf{x}$. Note that sometimes one writes $S^\# = (S^\top S)^{-1} S^\top$ as the “pseudoinverse” of S , from which it would follow that $\mathbf{a}_x = S^\# \mathbf{x}$.

By expanding the single-vector AMF formulation (Sec. 3.1) to account for a target subspace representation, we have that subspace AMF computes the length of \mathbf{x} when projected into the subspace S . This is given by the length of the projection operator when applied to \mathbf{x} , that is

$$\begin{aligned} \text{ss-AMF: } \mathcal{D}(\mathbf{x}) &= \|P_s \mathbf{x}\| \\ &= \|S(S^\top S)^{-1} S^\top \mathbf{x}\| \\ &= \sqrt{\mathbf{x}^\top S(S^\top S)^{-1} S^\top S(S^\top S)^{-1} S^\top \mathbf{x}} \\ &= \sqrt{\mathbf{x}^\top S(S^\top S)^{-1} S^\top \mathbf{x}}. \end{aligned} \quad (6)$$

In the literature, this is also commonly known by the name “adaptive matched subspace detector.”^{41,42}

Similarly, by expanding the single-vector ACE formulation (Sec. 3.1) to account for a target subspace representation, we have that subspace ACE computes the squared cosine of the angle θ between \mathbf{x} and the subspace S . The angle between \mathbf{x} and the subspace is the same as the angle between \mathbf{x} and the closest member of the subspace, i.e., the angle between \mathbf{x} and $\mathbf{s} = P_s \mathbf{x} = S \mathbf{a}_x$. From Eq. (2) where $\mathcal{D}(\mathbf{x}) = (\mathbf{s}^\top \mathbf{x})^2 / [\|\mathbf{s}\|^2 \|\mathbf{x}\|^2]$, the subspace ACE detector is obtained by replacing \mathbf{s} in Eq. (2) with $P_s \mathbf{x}$

$$\begin{aligned} \text{ss-ACE: } & \mathcal{D}(\mathbf{x}) = \cos^2 \theta \\ &= \frac{([P_s \mathbf{x}]^\top \mathbf{x})^2}{\|P_s \mathbf{x}\|^2 \|\mathbf{x}\|^2} = \frac{(\mathbf{x}^\top P_s^\top \mathbf{x})(\mathbf{x}^\top \mathbf{x})}{(\mathbf{x}^\top P_s^\top P_s \mathbf{x})(\mathbf{x}^\top \mathbf{x})} \\ &= \frac{(\mathbf{x}^\top P_s \mathbf{x})^2}{(\mathbf{x}^\top P_s \mathbf{x})(\mathbf{x}^\top \mathbf{x})} = \frac{\mathbf{x}^\top P_s \mathbf{x}}{\mathbf{x}^\top \mathbf{x}} \\ &= \frac{\mathbf{x}^\top S(S^\top S)^{-1} S^\top \mathbf{x}}{\mathbf{x}^\top \mathbf{x}}. \end{aligned} \quad (7)$$

Geometrically, these are equivalent to

$$\text{ss-AMF: } \mathcal{D}(\mathbf{x}) = \|P_s \mathbf{x}\| = \|S \mathbf{a}_x\| \quad (8)$$

and

$$\text{ss-ACE: } \mathcal{D}(\mathbf{x}) = \frac{\|P_s \mathbf{x}\|^2}{\|\mathbf{x}\|^2} = \frac{\|S \mathbf{a}_x\|^2}{\|\mathbf{x}\|^2}. \quad (9)$$

Note that although ss-AMF [Eq. (6)] has a square root, it is strictly positive. So even if it were squared, the detector would be strictly equivalent, as the rank order of the detections would not change. As with one-sided single-spectrum ACE (i.e., ACE⁺), single-spectrum AMF is signed, but the corresponding subspace variants are not signed. This is because of the linear subspace model, which cannot distinguish between positive and negative target directions; all possible linear combinations of the reference targets are considered to represent the target space. This holds for both AMF and ACE.

Another way to perform target detection with multiple input targets is to utilize a single-input detector in parallel over all possible targets, taking the maximum detection score for each pixel.⁴³ That is, for a set S of k library targets,

$$\text{max -AMF: } \mathcal{D}(\mathbf{x}) = \max_{s_k \in S} \{\mathcal{D}_{\text{AMF}}(\mathbf{x})\} = \max_{s_k \in S} \left\{ \frac{\mathbf{s}_k^\top \mathbf{x}}{\|\mathbf{s}_k\|} \right\} \quad (10)$$

and

$$\text{max -ACE: } \mathcal{D}(\mathbf{x}) = \max_{s_k \in S} \{\mathcal{D}_{\text{ACE}^+}(\mathbf{x})\} = \max_{s_k \in S} \left\{ \frac{\mathbf{s}_k^\top \mathbf{x}}{\|\mathbf{s}_k\| \|\mathbf{x}\|} \right\}. \quad (11)$$

Note that just as ss-ACE is equivalent to max-ACE when applied to all elements of the subspace, simplex-ACE is equivalent to max-ACE when applied to all elements of the constrained subspace. The same holds for max-AMF with respect to both ss-AMF and simplex-AMF.

As a baseline, we consider a very straightforward way to perform target detection with multiple input targets, which is

to use a standard single-input detector with the average spectrum as the single input target. For a target subspace S , the average target spectrum is given by $\boldsymbol{\mu}_S = (1/k)S\mathbf{1}$, where $\mathbf{1} \in \mathbb{R}^k$ is a vector of all ones. The average detectors for AMF [Eq. (1)] and ACE⁺ [Eq. (3)] are then given by

$$\text{avg-AMF: } \mathcal{D}(\mathbf{x}) = \frac{\boldsymbol{\mu}_S^\top \mathbf{x}}{\|\boldsymbol{\mu}_S\|} \quad (12)$$

and

$$\text{avg-ACE: } \mathcal{D}(\mathbf{x}) = \frac{\boldsymbol{\mu}_S^\top \mathbf{x}}{\|\boldsymbol{\mu}_S\| \|\mathbf{x}\|}. \quad (13)$$

When the magnitude of the variability is small, and all the signatures are very similar, avg-ACE in particular is expected to behave reasonably, although there is the possibility that it could average out important spectral features: the average of highly variable targets may result in a spectrum that does not look like the target at all. In any case, because it effectively ignores target variability, it provides a useful point of comparison for algorithms that are designed to take variability into account.

3.3 Simplex Detectors

In the simplex detector formulation, instead of computing the angle between \mathbf{x} and the full linear target subspace S , we compute the angle between \mathbf{x} and the constrained target subspace E . In place of the subspace S , we let E be the matrix of target endmembers (as columns) that define the edges of the target simplex. In this construct, we do not enforce a sum-to-one constraint; we are applying this to AMF and ACE, and for those detectors, the magnitude of the target signature does not matter. It bears remarking that because we are not enforcing a sum-to-one constraint, this is more of a “simplex cone” than a simplex in the usual sense of the word, but we use the term simplex for the sake of brevity; the mathematical term for an “uncapped” simplex, or one without a summation constraint, is a k -dimensional polyhedral cone with k edges.⁴⁴ The true constraint here is with respect to the abundances; that is, we are only allowing non-negative linear combinations of the target endmembers (whereas the subspace formulation allows for all linear combinations of the targets). In constraining this target subspace to a simplex, we obtain a target space representation that is less sensitive to noise and spectral library size. Colloquially, as target spectra vary even slightly, the size of the linear subspace will grow dramatically; in contrast, the target simplex will only expand slightly to account for this variability.

We define the abundance vectors as

$$\mathbf{a}_x = \operatorname{argmin}_{\mathbf{a}} \|\mathbf{x} - E\mathbf{a}\| \quad \text{such that } \mathbf{a} \geq 0. \quad (14)$$

By combining Eq. (14) with Eqs. (8) and (9), it follows that the simplex AMF and simplex ACE detectors are given by

$$\text{simplex-AMF: } \mathcal{D}(\mathbf{x}) = \|E\mathbf{a}_x\| \quad (15)$$

and

$$\text{simplex-ACE: } \mathcal{D}(\mathbf{x}) = \frac{\|E\mathbf{a}_x\|^2}{\|\mathbf{x}\|^2} = \cos^2 \phi, \quad (16)$$

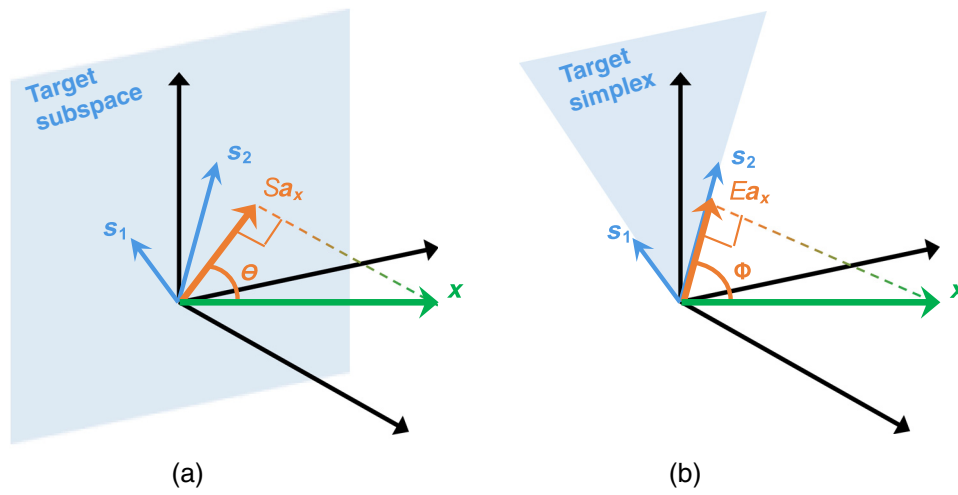


Fig. 1 Illustration of the differences in computing the projection of the pixel-under-test \mathbf{x} onto the (a) target subspace S in ss-AMF and ss-ACE and (b) target simplex E in simplex-AMF and simplex-ACE. In this example, \mathbf{s}_1 and \mathbf{s}_2 are the target reference spectra.

where the simplex-AMF detection score is the length of \mathbf{x} when projected into the target simplex E , and the simplex-ACE detection score is the squared cosine of the angle ϕ between \mathbf{x} and the target simplex E . An illustration of the differences between computing an angle with respect to a target subspace and with respect to a target simplex is shown in Fig. 1.

In general, solving Eq. (14) is a quadratic programming problem, which makes the simplex detectors computationally

more complex than their subspace counterparts. However, it is the same quadratic programming problem that is routinely employed in hyperspectral unmixing,^{45,46} but without the sum-to-one constraint; the difference is that the endmembers are not “pure pixels” from the background but are characteristic target spectra. The results here were generated using Python implementations, with pseudocode provided in Algorithm 1.

Algorithm 1 Simplex detectors: python pseudocode.

```

function SIMPLEX_AMF (image  $X$ , targets  $E$ )
    Compute  $R$  = covariance of  $X$ 
     $X \leftarrow R^{-1/2}X$                                       $\triangleright$  we use NUMPY.COV
     $E \leftarrow R^{-1/2}E$                                       $\triangleright$  whiten  $X, E$ 
    for pixel  $\mathbf{x}_i$  in  $X$  do
         $\mathbf{a}_x \leftarrow \arg \min_{\mathbf{a}} \|\mathbf{x}_i - E\mathbf{a}\|$  such that  $\mathbf{a} \geq 0$            $\triangleright$  we use SCIPY.OPTIMIZE.NNLS
        scores[i] =  $\|E\mathbf{a}_x\|$ 
    end for
    return scores
end function

function SIMPLEX_ACE (image  $X$ , targets  $E$ )
    Compute  $R$  = covariance of  $X$ 
     $X \leftarrow R^{-1/2}X$                                       $\triangleright$  we use NUMPY.COV
     $E \leftarrow R^{-1/2}E$                                       $\triangleright$  whiten  $X, E$ 
    for pixel  $\mathbf{x}_i$  in  $X$  do
         $\mathbf{a}_x \leftarrow \arg \min_{\mathbf{a}} \|\mathbf{x}_i - E\mathbf{a}\|$  such that  $\mathbf{a} \geq 0$            $\triangleright$  we use SCIPY.OPTIMIZE.NNLS
        scores[i] =  $\|E\mathbf{a}_x\|^2 / \|\mathbf{x}_i\|^2$ 
    end for
    return scores
end function

```

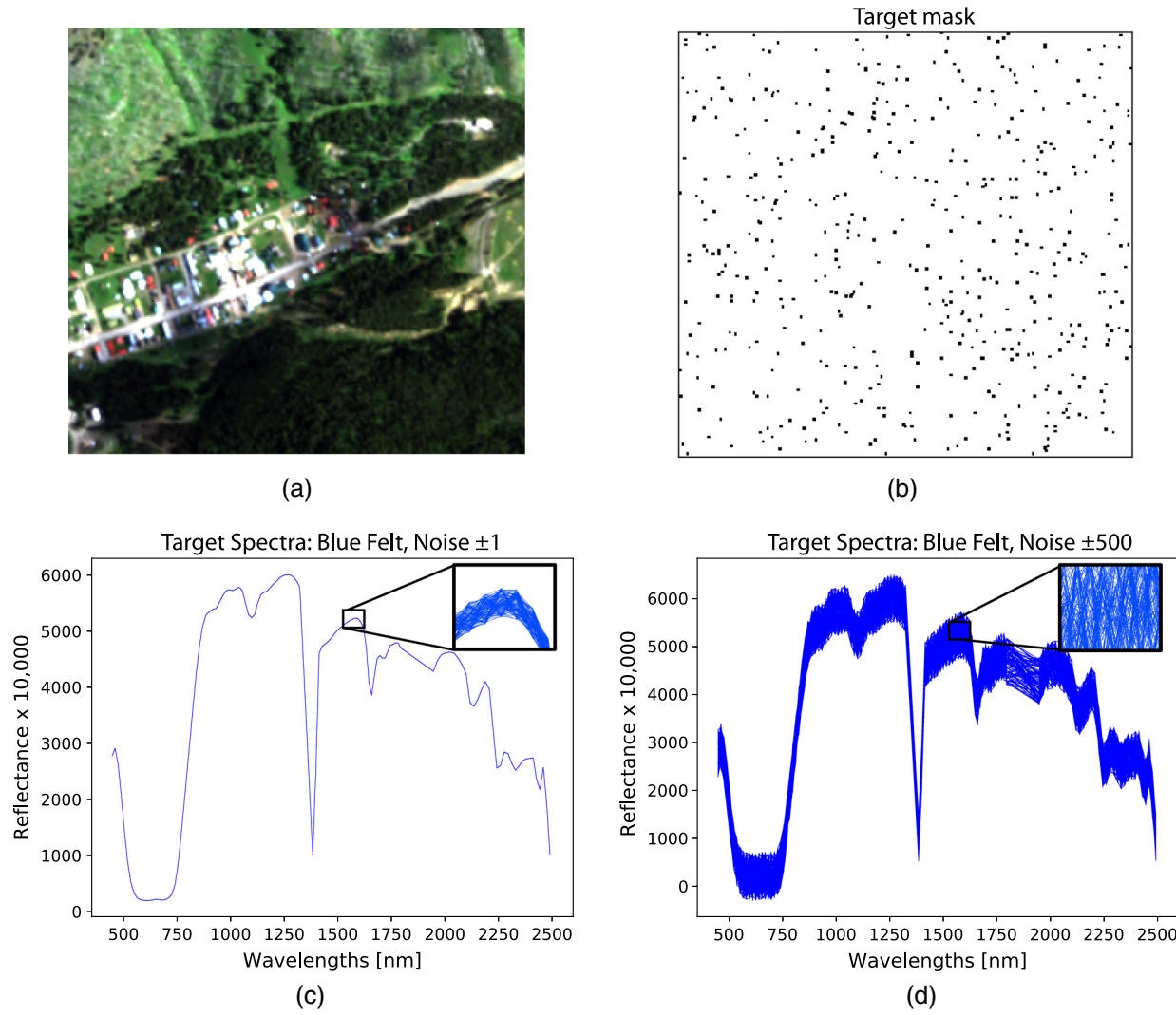


Fig. 2 Data used to generate the implanted target dataset. (a) RGB of the hyperspectral image over Cooke City, Montana. (b) Target mask showing the 500 locations for the implanted targets. (c) Sample target spectra generated by duplicating the blue felt spectrum and adding uniform random noise with amplitude 1 and (d) amplitude 500.

4 Experiments and Results

These experiments were conducted for both implanted targets and ground-truthed data. For each experiment, performance results are compared for a suite of AMF detectors (simplex-AMF, ss-AMF, max-AMF, and avg-AMF) and ACE detectors (simplex-ACE, ss-ACE, max-ACE, and avg-ACE).

4.1 Implanted Targets

The implanted target dataset was created using (i) an aerial hyperspectral image of Cooke City, Montana and (ii) an ASD spectrometer-measured target spectrum of blue felt (see Fig. 2). The Cooke City image was collected as part of the “blind test” dataset by Rochester Institute of Technology (RIT),⁴⁷ and a 280×300 pixel subset is used here. It was imaged by the HyMap sensor and is VNIR-SWIR with 126 bands. The image and the spectrum are in reflectance (scaled by 10,000).

The single target spectrum of blue felt was used to populate both implanted target images and simulated spectral libraries. This was done by duplicating the spectrum, and then adding some amount of uniform random noise to each element of each duplicate. This roughly mimics the situation

in which materials such as grass exhibit a texture in the image, with each pixel exhibiting a slightly different spectrum. We repeated this for two noise amplitudes (1 and 500) across two library sizes (10 targets and 100 targets). For a given noise amplitude and library size, (i) 500 noisy variants of the blue felt spectrum were generated and then implanted into the 500 target locations in the image, each of which was mixed to be a subpixel target with at most 5% target abundance, and (ii) 10 (or 100) additional noisy variants were generated for the library targets.

We looked in detail at detector performance (i.e., ROC curves and detection maps) as we increased the number of targets while keeping the noise amplitude fixed. For our first case, the added noise ranged between -1 and 1 ; because we worked in reflectance scaled by 10,000, this noise amounted to just one part in 10,000 or 0.01% reflectance. After populating the implanted image with 500 noisy target variants, we generated 10 more variants for our library and then ran the eight detectors. We then generated a larger library with 100 new noisy variants and again ran the eight detectors. The two sets of results are shown in Fig. 3. This is

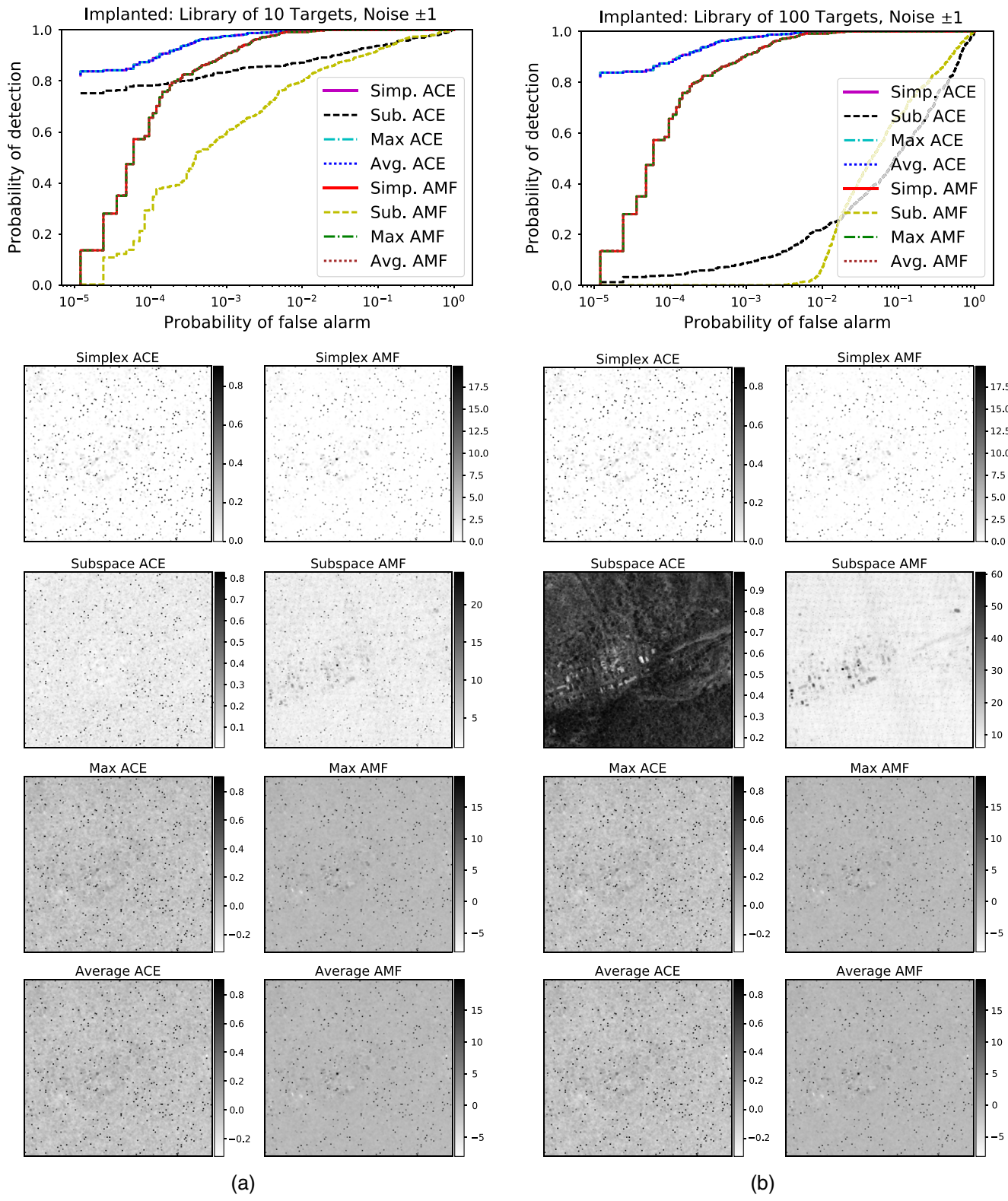


Fig. 3 Results for the implanted data with noise ± 1 , and target libraries with (a) 10 targets and (b) 100 targets. In this case, the targets have very low amplitude variability. Note that the simplex, average, and max variants of ACE show identical performance; this is similarly true for the simplex, average, and max variants of AMF.

an extreme case to show how sensitive subspace detectors are to library size, and in turn how poorly ss-ACE and ss-AMF perform in this limit while the simplex/max/avg-ACE detectors and simplex/max/avg-AMF detectors remain

essentially equivalent to each other, respectively. For our second case, we performed the same experiment but with a higher amplitude noise level of 500 (which is 0.05 in terms of percent reflectance). The results are shown in Fig. 4.

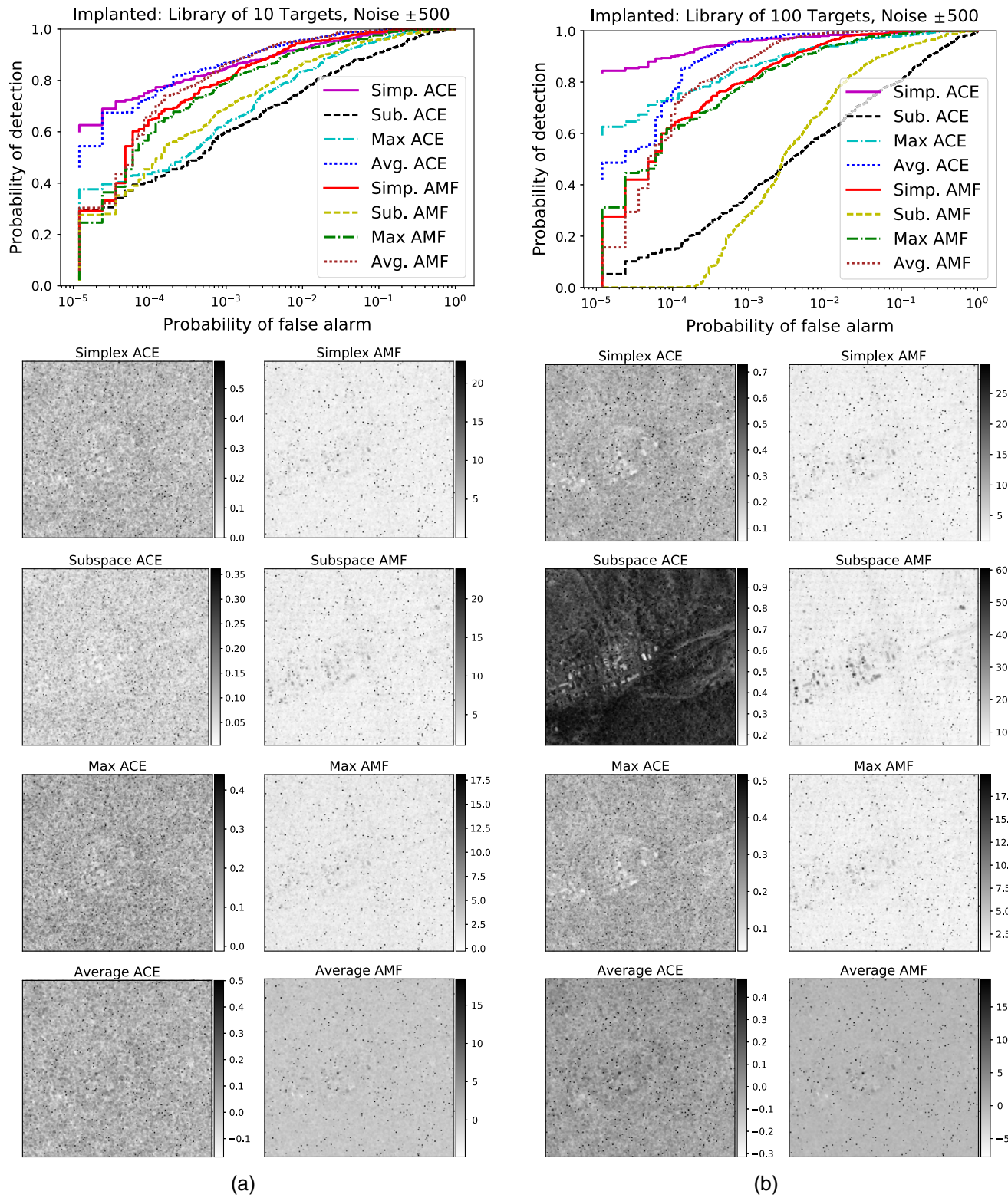


Fig. 4 Results for the implanted data with noise ± 500 , and target libraries with (a) 10 targets and (b) 100 targets.

As the number of targets increases for each amplitude, the detector performance of ss-ACE and ss-AMF degrades due to the growing dimension of the target subspace. In particular, ss-ACE exhibits a lot of false alarms as the size of the target library increases, which is evident in how dark

the detection maps are. In the limit as the subspace takes over the full image space, everything is detected as a target. As the amplitude of target variability increases, the detector performance of avg-ACE also degrades due to the averaging out of spectral features. At low false-alarm rates in these

cases, simplex-ACE performs as well as or better than the other detectors; the performance of simplex-ACE is most evident in Fig. 4(b) for the case of noise amplitude 500 with a spectral library of 100 targets. In that case, simplex-ACE is able to capture the variability of the target spectra well.

4.2 Ground-Truthed Targets

The ground-truthed target dataset is from RIT's SHARE 2012 campaign.⁴⁸ This multimodal campaign included a ground-truthed target detection experiment where felt panels were placed in various states of illumination and occlusion.⁴⁹ The aerial image was captured by the SpecTIR VS sensor, which is VNIR-SWIR with 360 bands. After bad band removal, the image had 229 bands. The ground sample distance of the sensor was ~ 1 m, and the georectified image used here is 170×280 pixels and is atmospherically compensated to approximate ground-surface reflectance.

In this experiment, the targets were red and blue felt cotton panels in both $2\text{ m} \times 2\text{ m}$ and $3\text{ m} \times 3\text{ m}$ sizes. The panels were deployed to generate a dataset containing subpixel targets, full pixel targets, shadowed and fully illuminated targets, and partially occluded targets. The target spectra in the spectral library were obtained from multiple sources: lab-measurements, field-measurements, in-scene pixels from another hyperspectral dataset where these targets were deployed (the SHARE 2010 collect⁵⁰), and a couple of obvious, bright in-scene target pixels in the image itself. We wanted to mimic a true spectral library as much as possible, which typically includes any and all available target spectra, and it is often the case that known in-scene target pixels are used to search the rest of an image for further

target occurrences. This resulted in a spectral library containing 146 red felt spectra and 170 blue felt spectra. The image and spectra are shown in Fig. 5.

The results of this experiment are shown in Figs. 6–8. We have three cases: using the 146 red felt spectra to detect the red felt panels, using the 170 blue felt spectra to detect the blue felt panels, and using the 316 red and blue felt spectra to simultaneously detect both the red and blue felt panels. The simplex-ACE detection results consistently outperform ss-ACE. The avg-ACE detection results are poor, as expected, due to the high degree of variability in these real target spectra. In these experiments, max-ACE was very competitive with simplex-ACE.

5 Conclusions

For target materials that are best described using a spectral library, subspace detectors are often used. This generally works well if the target subspace is small, but that conflicts with the utility of large spectral database libraries. As the target library grows, the target subspace will eventually overwhelm the image subspace, leading to the inability to discriminate between target and background, and subsequent false detections. In this paper, we have presented and derived simplex ACE, a target detector that instead uses a constrained subspace to represent the target space. For completeness, we have also derived simplex AMF and included the suite of both ACE and AMF detectors in the experiments. In the results, simplex ACE shows stable detection performance even as (i) the amplitude of the target variability increases and (ii) the number of target spectra increases. For the same experiments, subspace ACE shows greater

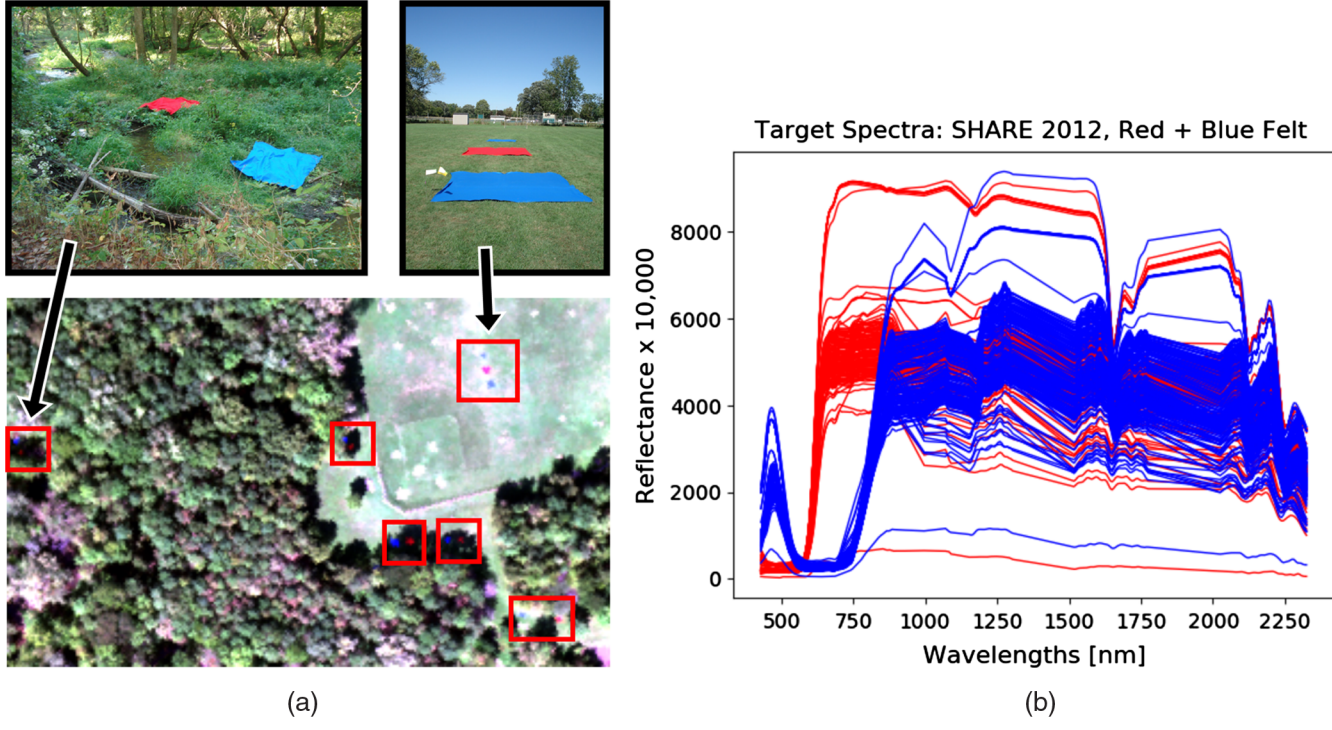


Fig. 5 The SHARE 2012 dataset. (a) RGB image showing known target locations in the red boxes, as well as ground photos of two of the target locations. (b) Library of target spectra (146 red and 170 blue) corresponding to the red and blue felt panels.

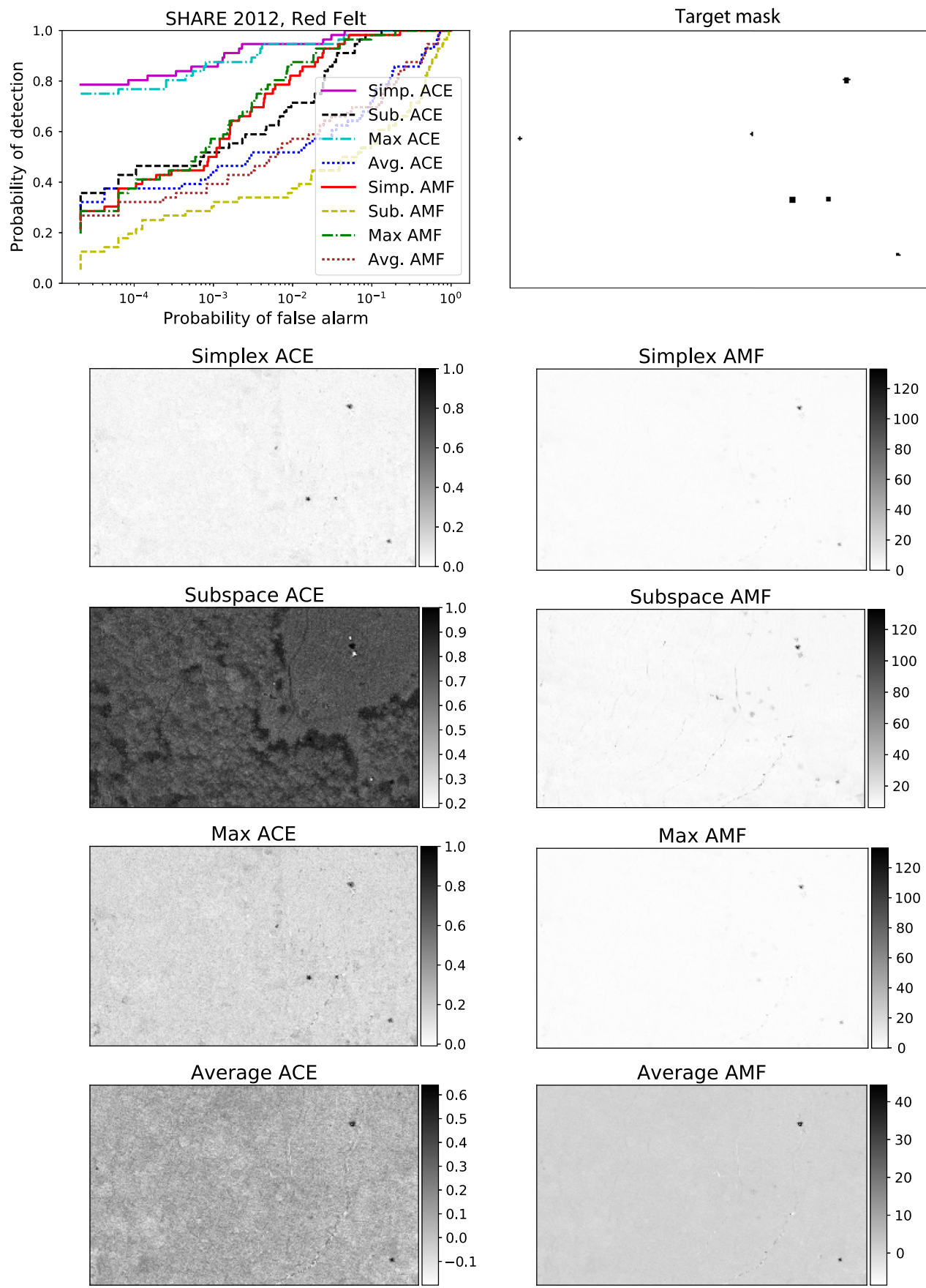


Fig. 6 Results for the SHARE 2012 dataset when detecting red felt. The target library had 146 spectra.

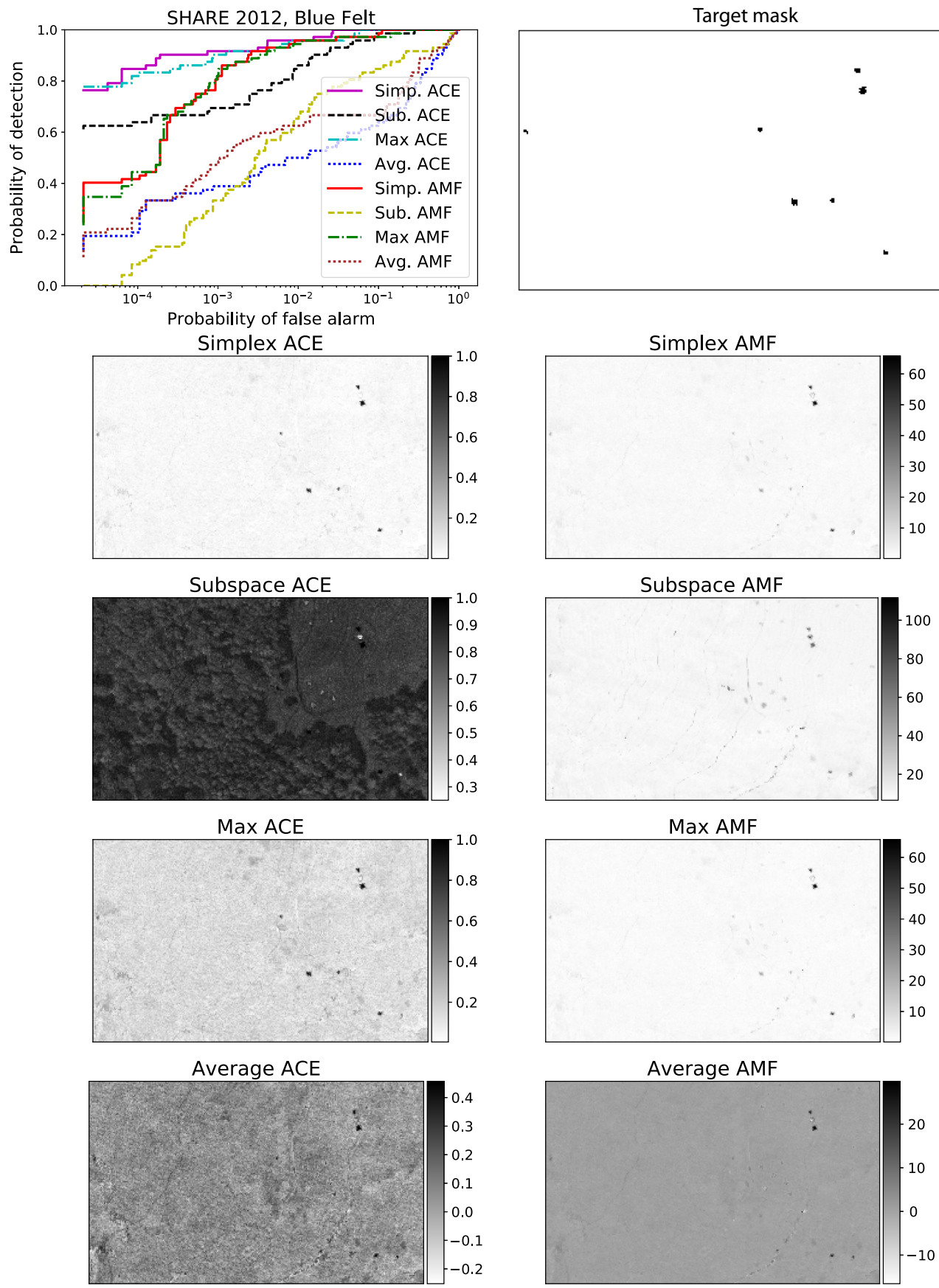


Fig. 7 Results for the SHARE 2012 dataset when detecting blue felt. The target library had 170 spectra.

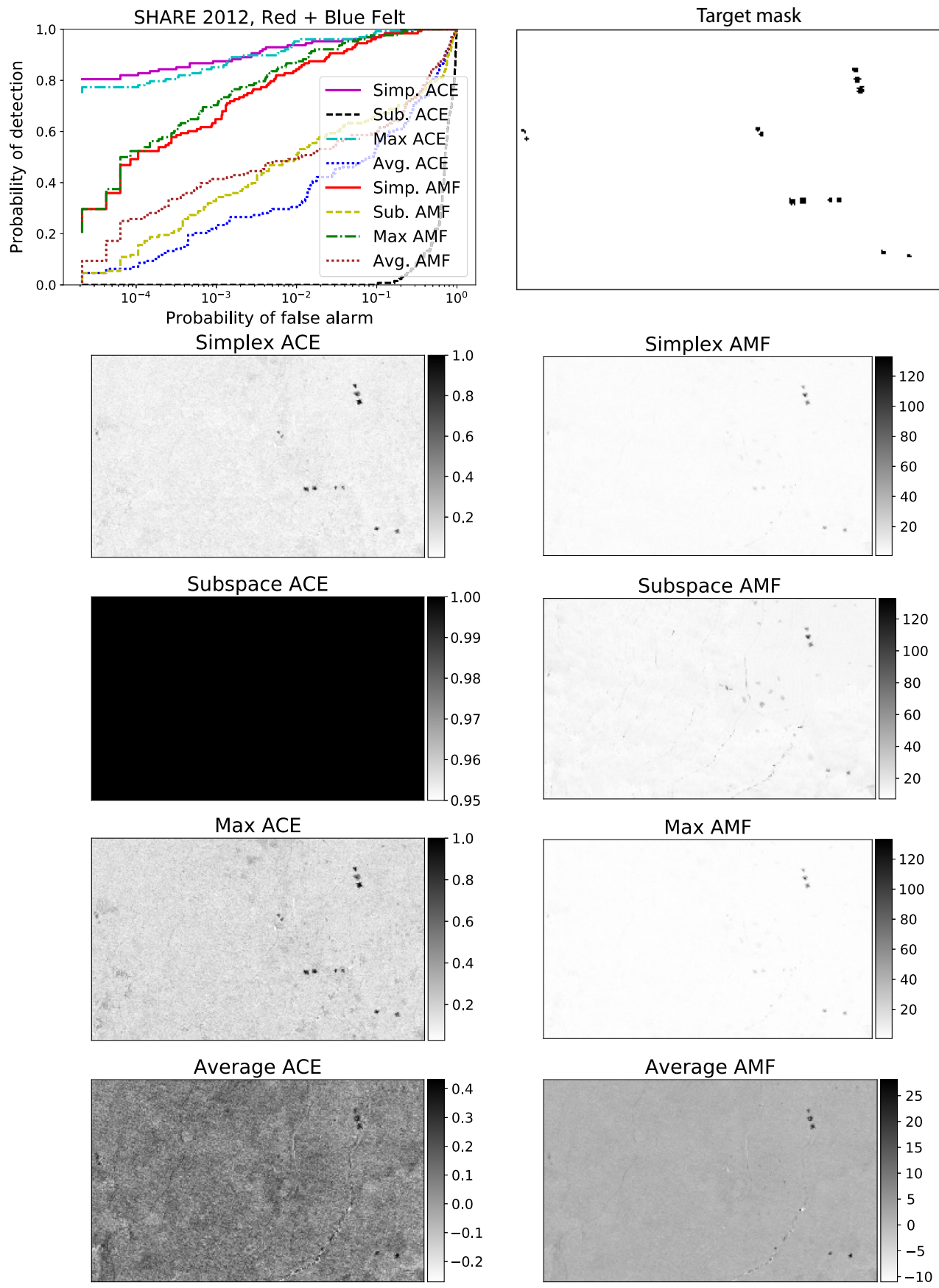


Fig. 8 Results for the SHARE 2012 dataset when detecting both red and blue felt. The target library had 316 spectra.

sensitivity to the number of target spectra. For many target signatures that are infinitesimally close to a central signature, simplex ACE reduces to standard ACE (in the false-alarm rate <0.5 regime). In general, simplex ACE provides a middle ground between traditional ACE (which does not make use of multiple target signatures) and subspace ACE (which can be overwhelmed by too many target signatures, in particular when the number of signatures begins to approach the number of spectral channels).

Acknowledgments

This research was supported by the U.S. Department of Energy (DOE) National Nuclear Security Administration (NNSA) Office of Defense Nuclear Nonproliferation. The project grant number is PL14-V-HARD solids-PD3WA. We are grateful to Emmett Lentilucci for providing data (and advice on interpreting that data) from the SHARE 2010 and SHARE 2012 campaigns. We also thank Steven Adler-Golden for useful conversations on constrained subspaces, and for pointing us to Ref. 17. The authors have no potential conflicts of interest to disclose.

References

- C. L. Bennett et al., "Infrared hyperspectral imaging results from vapor plume experiments," *Proc. SPIE* **2480**, 435 (1995).
- A. Hayden, E. Niple, and B. Boyce, "Determination of trace-gas amounts in plumes by the use of orthogonal digital filtering of thermal-emission spectra," *Appl. Opt.* **35**, 2802–2809 (1996).
- B. R. Foy, H. A. Fry, and B. D. McVey, "Approaches to chemical plume detection in hyperspectral infrared imaging," Tech. Rep. LA-CP-03-0103, Los Alamos National Laboratory (2003).
- J. Theiler, B. R. Foy, and A. M. Fraser, "Characterizing non-Gaussian clutter and detecting weak gaseous plumes in hyperspectral imagery," *Proc. SPIE* **5806**, 182 (2005).
- C. M. Gittins, "Detection and characterization of chemical vapor fugitive emissions by nonlinear optimal estimation: theory and simulation," *Appl. Opt.* **48**, 4545–4561 (2009).
- S. Matteoli, E. Lentilucci, and J. Kerekes, "Operational and performance considerations of radiative-transfer modeling in hyperspectral target detection," *IEEE Trans. Geosci. Remote Sens.* **49**, 1343–1355 (2011).
- T. Perkins et al., "High-speed atmospheric correction for spectral image processing," *Proc. SPIE* **8390**, 83900V (2012).
- S. Matteoli, M. Diani, and J. Theiler, "An overview background modeling for detection of targets and anomalies in hyperspectral remotely sensed imagery," *IEEE J. Sel. Top. Appl. Earth Obs. Remote Sens.* **7**, 2317–2336 (2014).
- M. Eismann, "Strategies for hyperspectral target detection in complex background environments," in *Proc. Aerospace Conf.*, IEEE (2006).
- T. L. Myers et al., "Quantitative reflectance spectra of solid powders as a function of particle size," *Appl. Opt.* **54**, 4863–4875 (2015).
- A. K. Ziemann and J. Theiler, "Material detection in hyperspectral imagery in support of nuclear nonproliferation," in *Proc. of Advances in Nuclear Nonproliferation Technology and Policy Conf.*, American Nuclear Society (2016).
- A. Ziemann and J. Theiler, "Graph-based and statistical approaches for detecting spectrally variable target materials," *Proc. SPIE* **9840**, 98400T (2016).
- A. Schaum, "Spectral subspace matched filtering," *Proc. SPIE* **4381**, 1–17 (2001).
- D. Manolakis, D. Marden, and G. Shaw, "Hyperspectral image processing for automatic target detection applications," *Lincoln Lab. J.* **14**(1), 79–116 (2003).
- J. R. Schott, *Remote Sensing: The Image Chain Approach*, Oxford University Press, Oxford (2007).
- D. Manolakis, R. Lockwood, and T. Cooley, *Hyperspectral Imaging Remote Sensing: Physics, Sensors, and Algorithms*, Cambridge University Press, Cambridge (2016).
- S. Adler-Golden, J. Gruninger, and R. Sundberg, "Hyperspectral detection and identification with constrained target subspaces," in *IEEE Int. Geoscience and Remote Sensing Symp. (IGARSS 2008)*, pp. 465–468 (2008).
- J. Broadwater, R. Meth, and R. Chellappa, "A hybrid algorithm for subpixel detection in hyperspectral imagery," in *Proc. IEEE Int. Geoscience and Remote Sensing Symp. (IGARSS 2004)*, Vol. 3, pp. 1601–1604 (2004).
- J. Broadwater and R. Chellappa, "Hybrid detectors for subpixel targets," *IEEE Trans. Pattern Anal. Mach. Intell.* **29**, 1891–1903 (2007).
- N. Longbotham et al., "Very high resolution multiangle urban classification analysis," *IEEE Trans. Geosci. Remote Sens.* **50**, 1155–1170 (2012).
- A. Villa et al., "Unsupervised methods for the classification of hyperspectral images with low spatial resolution," *Pattern Recognit.* **46**, 1556–1568 (2013).
- D. W. Messinger et al., "Metrics of spectral image complexity with application to large area search," *Opt. Eng.* **51**, 036201 (2012).
- J. Theiler and A. K. Ziemann, "Right spectrum in the wrong place: a framework for local hyperspectral anomaly detection," in *Proc. Computational Imaging XIV* (2016).
- C. Olson and T. Doster, "A parametric study of unsupervised anomaly detection performance in maritime imagery using manifold learning techniques," *Proc. SPIE* **9840**, 984016 (2016).
- J. Theiler et al., "Elliptically-contoured distributions for anomalous change detection in hyperspectral imagery," *IEEE Geosci. Remote Sens. Lett.* **7**, 271–275 (2010).
- A. Ziemann, D. Messinger, and B. Basener, "Iterative convex hull volume estimation in hyperspectral imagery for change detection," *Proc. SPIE* **7695**, 769511 (2010).
- D. Manolakis et al., "Detection algorithms in hyperspectral imaging systems: an overview of practical algorithms," *IEEE Signal Process. Mag.* **31**, 24–33 (2014).
- S. Zou and A. Zare, "Instance influence estimation for hyperspectral target signature characterization using extended functions of multiple instances," *Proc. SPIE* **9840**, 98400S (2016).
- A. Schaum, "Continuum fusion: a theory of inference, with applications to hyperspectral detection," *Opt. Express* **18**, 8171–8181 (2010).
- C. E. Caefer et al., "Improved covariance matrices for point target detection in hyperspectral data," *Opt. Eng.* **47**, 076402 (2008).
- A. Ziemann and D. W. Messinger, "An adaptive locally linear embedding manifold learning approach for hyperspectral target detection," *Proc. SPIE* **9472**, 947200 (2015).
- A. Ziemann, "Local spectral unmixing for target detection," in *Proc. Southwest Symposium on Image Analysis and Interpretation (SSIAI)*, IEEE (2016).
- A. Schaum, "Enough with the additive target model," *Proc. SPIE* **9088**, 90880C (2014).
- J. Theiler and A. Ziemann, "Local background estimation and the replacement target model," *Proc. SPIE* **10198**, 101980V (2017).
- I. S. Reed, J. D. Mallett, and L. E. Brennan, "Rapid convergence rate in adaptive arrays," *IEEE Trans. Aerosp. Electron. Syst.* **AES-10**, 853–863 (1974).
- E. J. Kelly, "Performance of an adaptive detection algorithm: rejection of unwanted signals," *IEEE Trans. Aerosp. Electron. Syst.* **25**, 122–133 (1989).
- F. C. Robey et al., "A CFAR adaptive matched filter detector," *IEEE Trans. Aerosp. Electron. Syst.* **28**, 208–216 (1992).
- L. L. Scharf and L. T. McWhorter, "Adaptive matched subspace detectors and adaptive coherence estimators," in *Proc. Asilomar Conf. on Signals, Systems, and Computers* (1996).
- S. Kraut, L. L. Scharf, and R. W. Butler, "The adaptive coherence estimator: a uniformly most-powerful-invariant adaptive detection statistic," *IEEE Trans. Signal Process.* **53**, 427–438 (2005).
- M. L. Pieper et al., "Hyperspectral detection and discrimination using the ACE algorithm," *Proc. SPIE* **8158**, 815807 (2011).
- L. L. Scharf and B. Friedlander, "Matched subspace detectors," *IEEE Trans. Signal Process.* **42**, 2146–2157 (1994).
- B. Thai and G. Healey, "Invariant subpixel material detection in hyperspectral imagery," *IEEE Trans. Geosci. Remote Sens.* **40**(3), 599–608 (2002).
- E. J. Lentilucci and P. Bajorski, "Hyperspectral target detection in a whitened space utilizing forward modeling concepts," in *Proc. Workshop on Hyperspectral Image and Signal Processing: Evolution in Remote Sensing (WHISPERS)*, IEEE (2010).
- J. A. De Loera, R. Hemmecke, and M. Koppe, *Algebraic and Geometric Ideas in the Theory of Discrete Optimization*, Society for Industrial and Applied Mathematics (SIAM), Philadelphia (2012).
- J. M. Bioucas-Dias et al., "Hyperspectral unmixing overview: geometrical, statistical, and sparse regression-based approaches," *IEEE J. Sel. Top. Appl. Earth Obs. Remote Sens.* **5**, 354–379 (2012).
- M. Parente and A. Plaza, "Survey of geometric and statistical unmixing algorithms for hyperspectral images," in *Proc. Workshop on Hyperspectral Image and Signal Processing: Evolution in Remote Sensing (WHISPERS)*, pp. 1–4, IEEE (2010).
- D. Snyder et al., "Development of a web-based application to evaluate target finding algorithms," in *Proc. of Geoscience and Remote Sensing Symp. (IGARSS '08)*, IEEE (2008).
- A. Giannandrea et al., "The SHARE 2012 data campaign," *Proc. SPIE* **8743**, 87430F (2013).
- E. J. Lentilucci, "Target detection assessment of the SHARE 2010/2012 hyperspectral data collection campaign," *Proc. SPIE* **9472**, 94720H (2015).
- J. A. Herweg et al., "SpecTIR hyperspectral airborne Rochester experiment data collection campaign," *Proc. SPIE* **8390**, 839028 (2012).

Amanda Ziemann is an Agnew National Security Postdoctoral Fellow at Los Alamos National Laboratory. She received BS and MS degrees in applied mathematics from Rochester Institute of Technology in 2010 and 2011, respectively, and a PhD in imaging science from RIT as well in 2015. She is a member of the Machine Learning and Data Exploitation Team at LANL. Her current research interests include remote sensing, spectral imaging, graph-based modeling, and signal processing.

James Theiler is a scientist at Los Alamos National Laboratory. He received SB degrees in mathematics and in physics from MIT in 1981, and a PhD in physics from Caltech in 1987. He subsequently held appointments at UCSD, MIT Lincoln Laboratory, LANL, and the Santa Fe Institute. He joined the technical staff at Los Alamos in 1994 and was named a laboratory fellow in 2005. His current research interests include statistical modeling, machine learning, image processing, and remote sensing.